PNAS RESEARCH ARTICLE | CHEMISTRY

# Phenylthiol-BODIPY-based supramolecular metallacycles for synergistic tumor chemo-photodynamic therapy

Xiongjie Lin[a,1], Feng Chen[a,1], Xiujun Yu[b], Heng Wang[b], Huayu Qiu[a], Yang Li[a,2], Shouchun Yin[a,2], and Peter J. Stang[c,2]

Edited by Peidong Yang, University of California Berkeley University Health Services, Berkeley, CA; received March 10, 2022; accepted June 3, 2022

**The development of more effective tumor therapy remains challenging and has received widespread attention. In the past decade, there has been growing interest in synergistic tumor therapy based on supramolecular coordination complexes. Herein, we describe two triangular metallacycles (1 and 2) constructed by the formation of pyridyl boron dipyrromethene (BODIPY)–platinum coordination. Metallacycle 2 had considerable tumor penetration, as evidenced by the phenylthiol-BODIPY ligand imparting red fluorescent emission at ∼660 nm, enabling bioimaging, and transport visualization within the tumor. Based on the therapeutic efficacy of the platinum(II) acceptor and high singlet oxygen ($^1O_2$) generation ability of BODIPY, 2 was successfully incorporated into nanoparticles and applied in chemo-photodynamic tumor therapy against malignant human glioma U87 cells, showing excellent synergistic therapeutic efficacy. A half-maximal inhibitory concentration of 0.35 μM was measured for 2 against U87 cancer cells in vitro. In vivo experiments indicated that 2 displayed precise tumor targeting ability and good biocompatibility, along with strong antitumor effects. This work provides a promising approach for treating solid tumors by synergistic chemo-photodynamic therapy of supramolecular coordination complexes.**

coordination-driven self-assembly | supramolecular coordination complex | boron dipyrromethene | tumor therapy | chemo-photodynamic synergistic therapy

## Significance

Pt-containing complexes have been widely investigated for their potential for antitumor efficacy. Here we report two triangular metallacycles via the coordination of diplatinum(II) acceptors and phenoxy-boron dipyrromethene (BODIPY) or phenylthiol-BODIPY ligands. The triangular metallacycle with phenylthiol-BODIPY shows enhanced antitumor efficacy by the synergistic chemotherapy of platinum(II) ligand and photodynamic therapy of heavy-atom-functionalized BODIPY photosensitizer compared to individual single therapy. This study provides a foundation for further studies on the in vivo efficacy of synergistic chemo-photodynamic therapy for solid tumors.

The high morbidity and mortality of cancer have motivated the search for effective tumor therapy, which remains as a challenge in medicine. Currently, tumors are treated mainly by surgery, chemotherapy, and radiotherapy (1–4). Among the recent developments in diagnostic equipment and treatment technology, photodynamic therapy (PDT), which involves the use of photosensitizers and specific light activation, has emerged as an effective treatment modality (5–11). PDT relies on photosensitizing dyes to produce highly active singlet oxygen ($^1O_2$), which surrounds biological macromolecules and is toxic to the surrounding diseased tissue, thereby killing cancer cells in solid tumors (12). Compared with traditional chemotherapy, PDT shows potential as an efficient approach for tumor therapy because of its fewer side effects, minimal damage to normal tissues, and negligible drug resistance (13). Photosensitizers play a vital role in determining the therapeutic effect of PDT. Among these, boron dipyrromethene (BODIPY) derivatives have received wide attention compared to other fluorescent dyes for use in PDT because of their $^1O_2$ generation ability and long fluorescence emission wavelength after simple modifications or coordination-driven self-assembly (2, 14–19). For example, introducing sulfur, and platinum(II) to BODIPY acting as heavy-atom/metal cannot only red-shift the absorption and fluorescence emission, but also promote $^1O_2$ generation, and boost the effect of PDT (14–20).

In recent decades, coordination-driven self-assembly has become a powerful tool for constructing supramolecular coordination complexes (SCCs) (20–25). Numerous discrete SCCs have been synthesized via the formation of metal-organic coordination bonds between electron-poor acceptors containing transition metals (Fe, Cu, Co, Zn, Pt, Pd, etc.) and rigid electron-rich donors (such as carboxylate, pyridine), including metallacycles and metallacages (26–35). By rational structure design and careful ratio control of acceptors and donors, SCCs with various geometries and different properties have been developed, which attracted great interest and showed wide application prospects in supramolecular polymers, host-guest chemistry, sensors, catalysts, amphiphilic self-assembly, and biomedicines (36–46). Furthermore, because of the excellent antitumor effects of Pt-containing complexes, SCCs based on Pt-coordination show potential for tumor therapy (47–49). For instance, a previous study described an elegant light-emitting metallacage, assembled using Pt as the metal nodes, with higher antitumor efficacy compared with clinical Pt-based drugs (50). Yu et al. (51) developed a fluorescent, self-assembled metallacycle to encapsulate doxorubicin as the chemotherapeutic drug for cell imaging and synergistic cancer therapy. Zhou et al. (52) designed a self-assembled BODIPY-Pt

Author affiliations: [a]College of Material, Chemistry and Chemical Engineering, Key Laboratory of Organosilicon Chemistry and Material Technology, Ministry of Education, Key Laboratory of Organosilicon Material Technology, Hangzhou Normal University, Hangzhou 310036, People's Republic of China; [b]College of Chemistry and Environmental Engineering, Shenzhen University, Shenzhen 518060, People's Republic of China; and [c]Department of Chemistry, University of Utah, Salt Lake City, UT 84112

Author contributions: Y.L. and S.Y. designed research; X.L., F.C., and Y.L. performed research; X.L., F.C., X.Y., H.W., H.Q., Y.L., and S.Y. analyzed data; and X.L., F.C., Y.L., S.Y., and P.J.S. wrote the paper.

The authors declare no competing interest.

This article is a PNAS Direct Submission.



[1]X.L. and F.C. contributed equally to this work.

[2]To whom correspondence may be addressed. Email: liyang@hznu.edu.cn, yinsc@hznu.edu.cn or stang@chem.utah.edu.

This article contains supporting information online at http://www.pnas.org/lookup/suppl/doi:10.1073/pnas.2203994119/-/DCSupplemental.

Published July 11, 2022.

supramolecular metallacycle for chemo-photodynamic therapy and reported excellent synergistic effects in A2780cis cells in vitro; however, no antitumor effect was observed in vivo. Thus, considering the superior antitumor effects of platinum(II) and $^1O_2$, the development of Pt-based SCCs using $^1O_2$ generating heavy-atom-functionalized BODIPY photosensitizers as functional building blocks with the goal of combining chemotherapy and PDT may enhance antitumor efficacy compared to individual single therapy.

In this work, we report two triangular metallacycles (**1** and **2**; Fig. 1) with $^1O_2$ generation ability, constructed via the coordination of diplatinum(II) acceptors and phenoxy-BODIPY or phenylthiol-BODIPY ligands. Because of its superior $^1O_2$ generation capability and longer maximum fluorescence emission

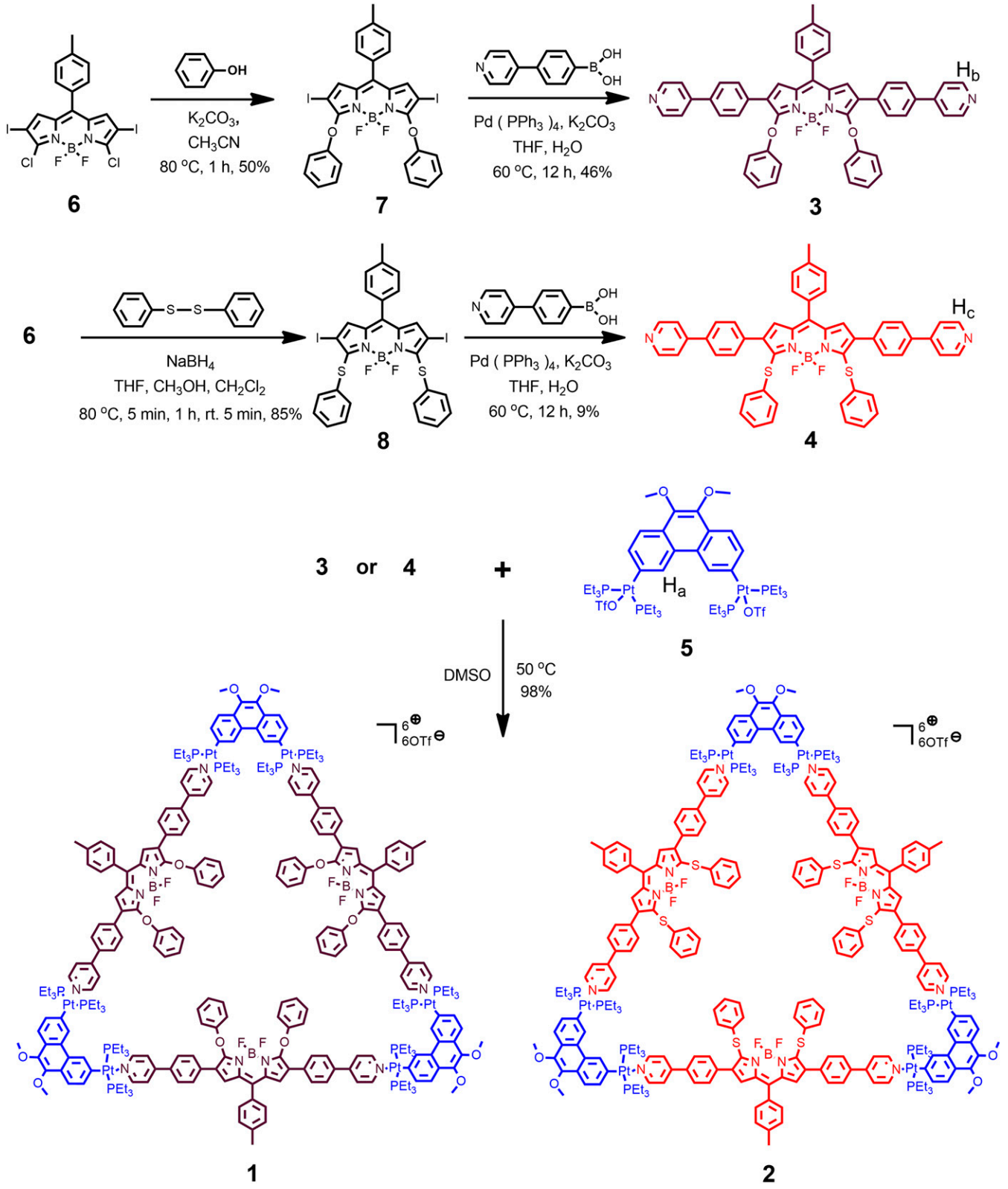


**Fig. 1.** Chemical structures and synthetic procedures of metallacycles (**1** and **2**), BODIPY ligands (**3** and **4**), and diplatinum acceptor (5).

wavelength, metallacycle **2** was further encapsulated by an amphiphilic polymer to prepare nanoparticles (NPs) for tumor therapy. The BODIPY ligands serve as the photosensitizer to generate $^1O_2$ to kill cancer cells under light irradiation, whereas the platinum(II) acceptors in the metallacycle enhance the therapeutic effect through strong antitumor effects. In vitro and in vivo experiments demonstrated that the synergistic combination of PDT and chemotherapy greatly enhanced the antitumor efficacy compared with single-treatment approaches. Moreover, the characteristic fluorescence of the BODIPY core within the metallacycle enabled imaging of the transport of therapeutic metallacycles by confocal microscopy.

## Results and Discussion

By applying a coordination-driven self-assembly method, the triangular metallacycles (**1** and **2**) were obtained in near quantitative yields (98% for both) by mixing 60° diplatinum(II) acceptor (5) and the corresponding BODIPY ligand (**3** or **4**) in a 1:1 ratio in dimethyl sulfoxide (DMSO) and stirring at 50 °C for 12 h. The detailed procedures for the synthesis of **3** and **4** are presented in *SI Appendix*, Figs. S1–S30. The structures of the triangular metallacycles were characterized using multinuclear NMR spectroscopy ($^1$H and $^{31}$P) and electrospray ionization time-of-flight mass spectrometry (ESI-TOF-MS). A sharp singlet peak was observed in the $^{31}$P NMR spectra of metallic triangles **1** and **2** at 13.70 ppm ($^1J_{Pt-P}$ = 2660 Hz; Fig. 1, spectrum *B*) and 13.80 ppm ($^1J_{Pt-P}$ = 2668 Hz; Fig. 2, spectrum *C*), indicating a single phosphorus environment. Relative to free platinum(II) acceptor **5** (Fig. 2, spectrum *A*), the peaks displayed upfield chemical shifts of 5.83 and 5.73 ppm for **1** and **2**, respectively, suggesting the coordination of the pyridyl groups to platinum(II) as well as the formation of a highly symmetrical structure. In the $^1$H NMR spectrum of metallacycle **1** (Fig. 2, spectrum *E*), the peaks related to the

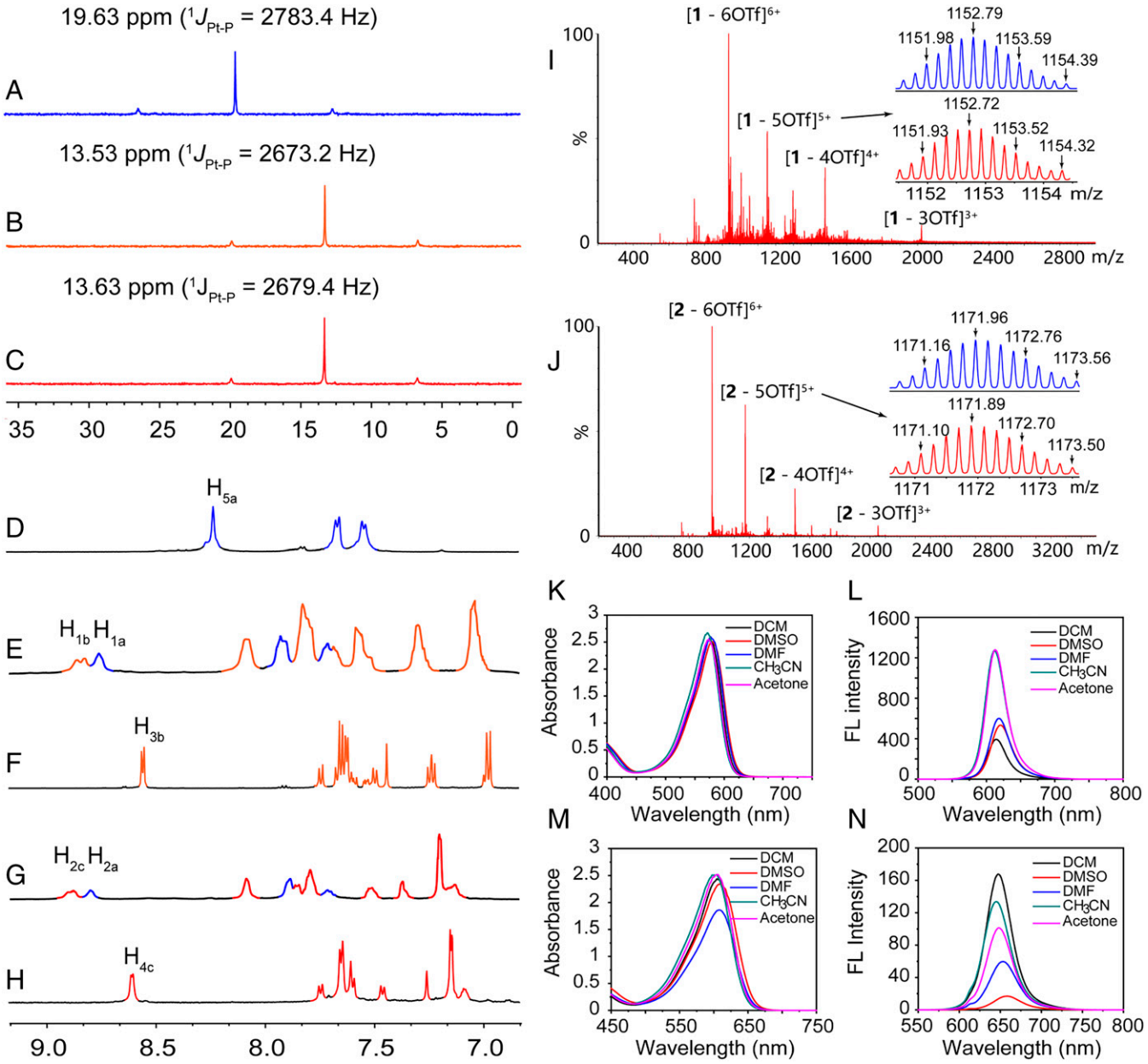


**Fig. 2.** (*A*–*C*) Partial $^{31}$P NMR ($CDCl_3/CD_2Cl_2$; 297 K) spectra and (*D*–*H*) $^1$H NMR spectra (DMSO-$d_6$; 297 K) of (*A* and *D*) the free 60° diplatinum(II) acceptor (5), (*F*) phenoxy-boron dipyrromethene (BODIPY) (3), (*H*) phenylthiol-BODIPY (4), (*B* and *E*) metallacycle **1**, and (*C* and *G*) metallacycle **2**. Experimental (red) and calculated (blue) ESI-TOF-MS spectra of (*I*) [**1** – 5OTf]$^{5+}$ and (*J*) [**2** – 5OTf]$^{4+}$. Absorption and fluorescence spectra of (*K* and *L*) metallacycle **1** and (*M* and *N*) metallacycle **2** in different solvents ($\lambda_{ex}$: 570 nm for **1** and 610 nm for **2**; *c* = 10 μM).

α-pyridyl protons $H_b$ displayed a downfield shift (from 8.62 to 8.88 ppm) compared to that of free BODIPY ligand **3** (Fig. 2, spectrum *F*). Similarly, a downfield chemical shift (from 8.66 to 8.91 ppm) of the α-pyridyl protons $H_c$ was observed in the $^1$H NMR spectrum of **2** (Fig. 2, spectrum *G*) in contrast to that of the free BODIPY ligand **4** (Fig. 2, spectrum *H*). Additionally, the signals corresponding to $H_a$ on the platinum(II) acceptor **5** (Fig. 2, spectrum *D*) shifted downfield (from 8.22 to 8.49 and 8.51 ppm) after the assembly of the metallacycle. These results support the formation of the triangular metallacycles. ESI-TOF-MS provided further evidence of the successful production of triangular metallacycles (53). For example, the mass spectrum of metallacycle **1** (Fig. 2, spectrum *I*) displayed four sets of mass peaks, from 3+ to 6+, representing the [3 + 3] assembled metallacycles with loss of different numbers of triflate counterions ($OTf^-$). A peak at $m/z = 1152.72$ representing the loss of five triflate counterions from **1** ($[\mathbf{1} - 5OTf]^{5+}$) was compared with the expected isotope pattern (Fig. 2, spectrum *I*), supporting the stoichiometric composition of the metallacycle. In the mass spectrum of metallacycle **2**, similar peaks were found and their isotropic distribution matched well with the calculated data (Fig. 2, spectrum *J*). In the 2D diffusion-ordered $^1$H NMR spectroscopy (DOSY) experiments, a single band was observed, confirming the formation of a single product (*SI Appendix*, Figs. S22 and S28). The diffusion coefficients of **1** and **2** were measured to be the same ($3.43 \times 10^{-11}$ $m^2/s$) because of their similar molecular size. Overall, these results indicated the successful self-assembly of the discrete metallacycles, **1** and **2**.

The optical properties of the BODIPY-based metallacycles were also investigated, including the UV-Vis absorption and fluorescence emission characteristics in different solvents. In the absorption spectra, similar absorption bands, at ∼570 and ∼610 nm for metallacycle **1** and **2**, respectively, were observed in different solvents (Fig. 2, spectra *K* and *M*, *SI Appendix*, Figs. S24 and S25), due to the $\pi$-$\pi^*$ transition of BODIPY moiety. In the emission spectra, the fluorescence maxima of **1** and **2** were observed at ∼610 and 645 nm (Fig. 2, spectrum *L* and *N*), respectively. However, the emission intensities varied according to the solvents used (Fig. 2, spectrum *H* and *I*). For example, in dimethylformamide and DMSO, metallacycle **1** and **2** displayed small red shifts in the fluorescence wavelength and a decrease in the fluorescence intensities, which may be attributed to the stability of the molecular excited-state and/or effect of strong polar solvents on electron transfer between the metal centers and ligands. The quantum yields ($\Phi_F$) of the BODIPY ligands and the metallacycles in different solvents were also measured (*SI Appendix*, Table S1; rhodamine B; $\Phi_F = 50\%$ in ethanol as the standard). The difference in the substituents greatly impacted the maximum fluorescence emission wavelength of the BODIPY ligands and metallacycles. **2**, with a structure based on phenylthiol-BODIPY, therefore has a longer fluorescence emission wavelength and lower quantum yield because of the introduction of a sulfur atom (a heavy atom), consistent with previous reports (14).

The $^1O_2$ generation ability of the metallacycles was then evaluated using electron paramagnetic resonance (EPR) with 2,2,6,6-tetramethyl-4-piperidone (TEMP) as the $^1O_2$ capturer. Characteristic triplet signals representing the oxidized TEMP were observed in the EPR spectra after light irradiation, indicating successful production of $^1O_2$ by the metallacycles (Fig. 3*B*). Metallacycle **2** displayed a much stronger $^1O_2$ generation ability than **1** under the same conditions. The generation of $^1O_2$ requires the triplet state of the photosensitizer; and the sulfur atom may promote the triplet transition of the metallacycle, thereby producing more $^1O_2$. The singlet oxygen quantum yield of metallacycle **2** was further measured using rose bengal (39%) as the standard

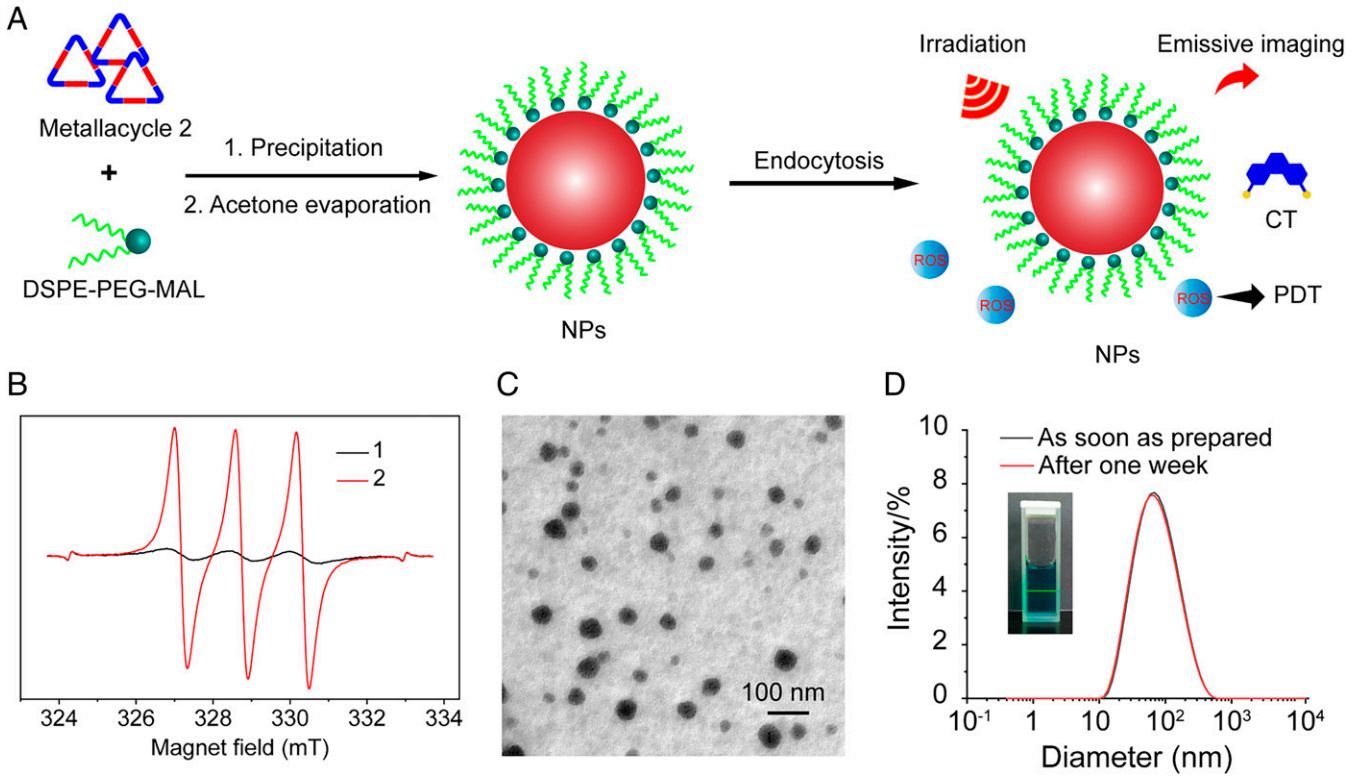


**Fig. 3.** (*A*) Nanoencapsulation method for preparing nanoparticles (NPs); CT, chemotherapy; DSPE-PEG-MAL, 1,2-distearoyl-*sn*-glycero-3-phosphoethanolamine-*N*-[maleimide(polyethylene glycol)-2000]; ROS, reactive oxygen species. (*B*) EPR spectra of metallacycles, **1** and **2**; the signals at both sides of the spectra represent the internal marker, $Mn^{2+}$. (*C*) TEM image and (*D*) dynamic light scattering (DLS) analysis of NPs (*Inset*: Tyndall effect of the aqueous NP solution).

(54, 55). The singlet oxygen quantum yield of metallacycle **2** was calculated to be 12.3% (*SI Appendix*, Fig. S31). Therefore, **2** was identified as a candidate for bioapplication.

NPs composed of polymers with good biocompatibility are a promising platform for disease diagnosis and treatment. Because of the hydrophobicity of the metallacycle and hydrophilic environment of living organisms, amphiphilic liposome 1,2-distearoyl-*sn*-glycero-3-phosphoethanolamine-*N*-[maleimide(polyethylene glycol)-2000] (DSPE-PEG-MAL) was used to encapsulate metallacycle **2**. The metallacycle-loaded NPs were obtained via the precipitation method (Fig. 3*A*). The aqueous NP solution exhibited a typical Tyndall effect (Fig. 3*D*; inset), demonstrating the formation of nanoaggregates. The size of NPs plays a pivotal role in their accumulation and retention in tumors. As such, the size and morphology of the NPs were determined using a transmission electron microscope (TEM) and dynamic light scattering. TEM revealed spherical, regular, and well-separated NPs with an average size of ∼50 nm (Fig. 3*C* and *D*). Dynamic light scattering indicated an average NP size of 49 nm in water, in agreement with the TEM measurement. This dimension corresponds with the reported optimal particle size (around 50 nm) for enhanced in vivo anticancer properties, e.g., stronger tumor inhibition and deeper tissue penetration. Additionally, the size distribution showed negligible changes after one week (Fig. 3*D*), suggesting good stability of the NPs in an aqueous environment.

The cytotoxicities of the NPs containing metallacycle **2** or BODIPY **4** were investigated in human embryonic kidney 293 cells (HEK293; Fig. 4*A*) and U87 glioblastoma cells (Fig. 4*B*) under light irradiation using a 3-(4′,5′-dimethylthiazol-2′-yl)-2,5-diphenyl tetrazolium bromide assay. Different concentrations of **2** and **4** in a NP solution displayed low toxicity toward U87 and HEK293 cells in the dark. However, under light irradiation, the viability of both cell types decreased gradually with increased concentrations of **2** and **4**. The half-maximal inhibitory concentrations ($IC_{50}$) of **4** and **2** against U87 cells were 2.49 and 0.35 μM, respectively. Thus, NPs containing metallacycle **2** displayed greater antitumor activity. Under the same conditions, the viability of U87 cells was lower than that of HEK293 cells, likely because of disassembly of the metallacycle in the acidic internal environment of U87 cancer cells, which resulted in release of the highly cytotoxic platinum acceptor.

To evaluate the generation of $^1O_2$ in cells after the internalization of NPs, dichlorofluorescein diacetate was selected as an oxidant-sensitive fluorescent dye, which exhibited green emission

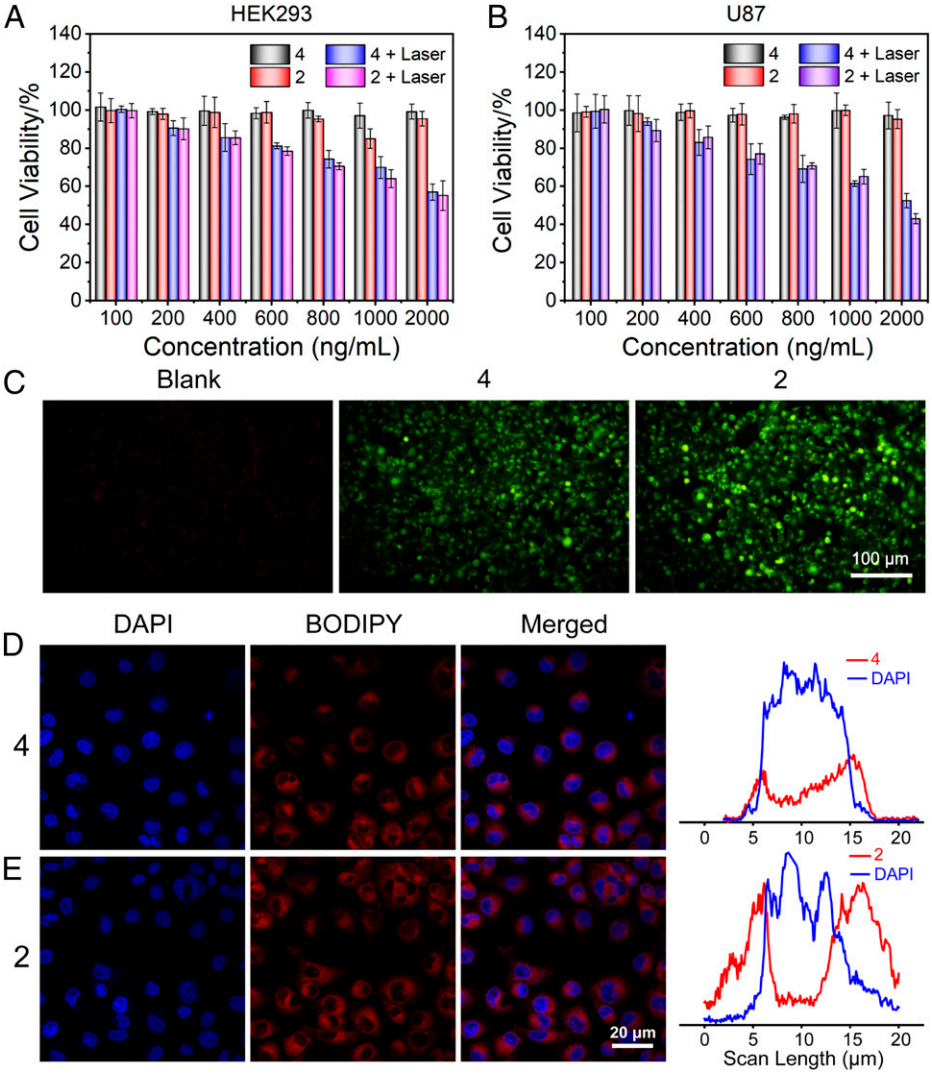


**Fig. 4.** Cell viability of (*A*) human embryonic kidney 293 (HEK293) cells and (*B*) U87 cells after treatment with **4** and **2** in the absence or presence of laser irradiation. (*C*) Confocal laser scanning microscopy images of untreated (blank) cells and cells treated with **4** or **2** in the presence of the singlet oxygen detector, dichlorofluorescin diacetate (DCF-DA) under light irradiation. Confocal laser scanning microscopy images and mean fluorescence intensities of human primary glioblastoma (U87) cells after incubation with (*D*) ligand **4** or (*E*) metallacycle **2**.

after oxidization to dichlorofluorescein by reactive oxygen species. NPs containing the metallacycle **2** or BODIPY **4** were internalized by U87 cells, which displayed typical green fluorescence attributed to dichlorofluorescein following light irradiation; in contrast, the blank group displayed no green fluorescence, suggesting efficient $^1O_2$ generation by **2** and **4** (Fig. 4*C*). A more pronounced green fluorescence was observed in the U87 cells treated with NPs containing the metallacycle **2** compared to other cells, indicating a higher intracellular concentration of $^1O_2$, possibly because of the higher intracellular accumulation of the metallacycles.

Cellular uptake and localization experiments were further conducted in vitro. Human malignant glioma cells (U87) were incubated at 37 °C with phenylthiol-BODIPY ligand **4** and metallacycle **2** for 24 h, respectively. Subsequently, confocal laser scanning microscopy was used to determine whether **2** and **4** were internalized by U87 cells, and counterstaining with 4′,6-diamidino-2-phenylindole (DAPI) was performed to differentiate nuclear and cytoplasmic areas. In the confocal laser scanning microscopy images (Fig. 4*D* and *E*), the cytoplasm of U87 cells showed strong red fluorescence after incubation, confirming that **2** and **4** were located mainly in the cytoplasm. U87 cells incubated with metallacycle **2** showed a strong red fluorescence, indicating a high cellular uptake rate of metallacycle **2** in U87 cells. This may be attributed to the electrostatic interaction between the positive metallacycle and negative cell membrane surface, which facilitated entry of the metallacycles.

The tumor accumulation efficacies were then monitored by recording fluorescence imaging of tumor sites at different times point (1 h, 2 h, 4 h, 8 h, 16 h, 24 h, 48 h) after intratumoural injection BODIPY **4** NPs and metallacycle 2 NPs, respectively. The fluorescence signal of the metallacycle **2** NPs at tumor tissues gradually increased with time. In vivo fluorescence imaging at 1 h postinjection showed that the metallacycle **2** NPs had higher fluorescence signal at tumor site than BODIPY **4** NPs. This signal persisted, even at postinjection times as long as 48 h, with a significant biodistribution of the metallacycle **2** NPs throughout the specimen (tumor and liver). In contrast, the fluorescence signal in the body annihilated much faster for the mice after administration of the BODIPY **4** NPs (Fig. 5*A* and *SI Appendix*, Fig. S32). Thus, metallacycle **2** can be applied for imaging-induced tumor therapy due to its strong and long-time fluorescence emission.

In order to evaluate the antitumor efficacy, U87 tumor-bearing mice were intraperitoneal injected with different formulations, including PBS, NPs containing BODIPY **4** and NPs containing metallacycle **2** (8 injections in 21 d; Fig. 5*B*). The tumor sites were irradiated using a 600–605 nm (60 mW cm$^{-2}$) laser for 10 min after 24 h of NPs injection. Control mice injected with PBS showed rapid tumor growth over time (Fig. 5*C* and *D*), with an average tumor volume of nearly 1000 mm$^3$ at the end of the experiment, whereas treatment with NPs containing **2** or **4** inhibited tumor growth. Accordingly, the tumor inhibition rate of NPs containing metallacycle **2** was calculated to be 66.6%, which was higher than that of NPs containing metallacycle **4** (27.8%), suggesting a better antitumor activity of NPs containing metallacycle **2**. In comparison with the structure of the metallacycle **2** and BODIPY **4**, it can be inferred that organoplatinum(II) in metallacycle **2** played a crucial role as the chemical antitumor drug, which was consistent with literature

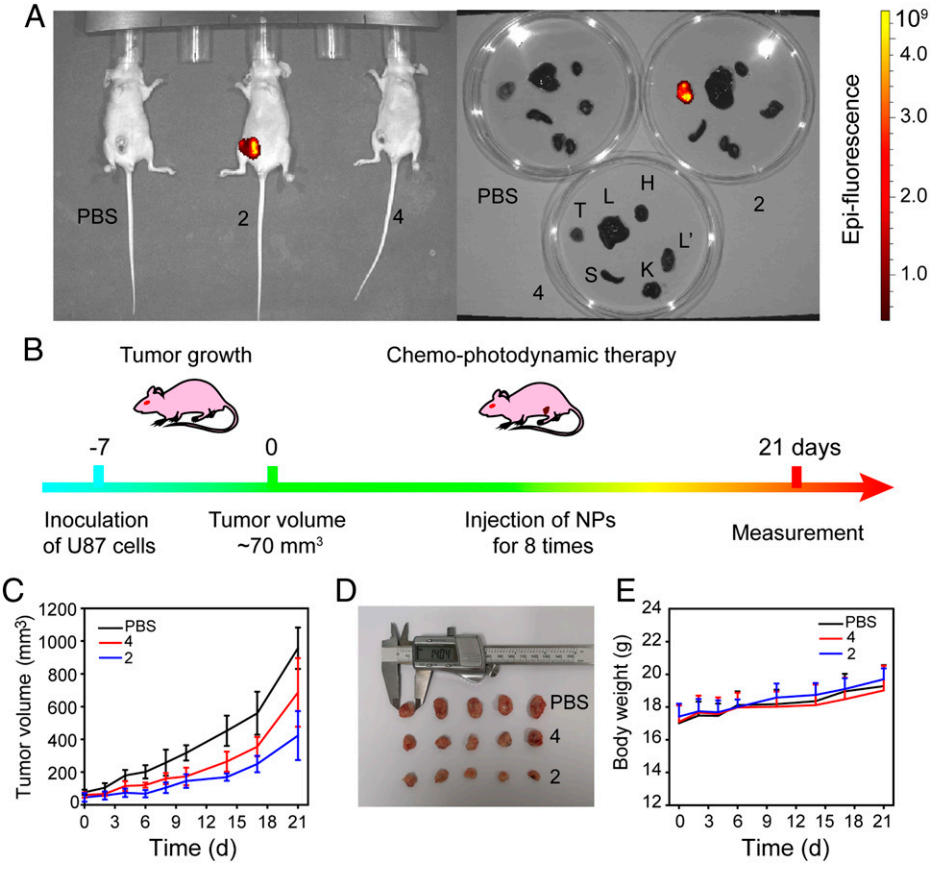


**Fig. 5.** (*A*) In vivo and ex vivo fluorescence images of the mice and their major organs at 24 h after the last injection (H: heart; L: liver; S: spleen; L′: lung; K: kidney; T: tumor). (*B*) Protocol of tumor therapy in mice inoculated with glioblastoma cells (U87); Variations in the (*C*) tumor volume and (*D*) body weight of mice during therapy; PBS, phosphate-buffered saline (control group); (*E*) gross appearance of the excised tumors at the end of the 21-d treatment period.

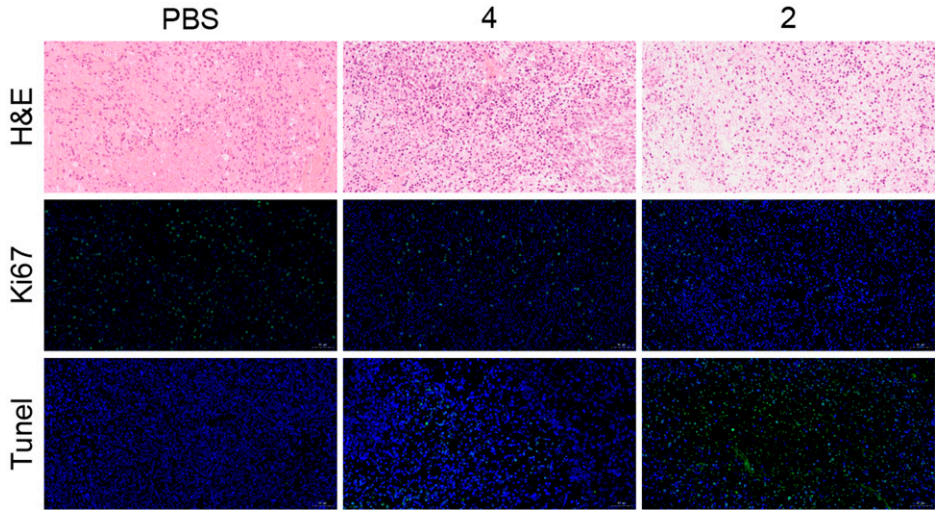


**Fig. 6.** H&E staining, Ki67 staining, and TUNEL images of tumor tissue sections from mice treated with phosphate-buffered saline (PBS), ligand **4**, or metallacycle **2** NPs.

reports (3, 50). Thus, an effective chemo-photodynamic synergistic effect was achieved in NPs containing metallacycle **2**. The therapeutic efficacy of NPs containing metallacycle **2** was also investigated by the hematoxylin-eosin (H&E) staining, nuclear nonhistone protein (Ki67) staining, and terminal deoxynucleotidyl transferase dUTP nick end labeling (TUNEL). After treatment of NPs containing metallacycle **2**, the greatest degree of nucleus–cytoplasm separation, the fewest green fluorescent dots representing the antigens secreted during cell proliferation, and the most abundant DNA disruption representing apoptosis was observed in the tumor cells, indicating a large inhibition of proliferative activity (Fig. 6).

Biosafety is an important concern in the application of NP-based therapy. Neither death nor any sign of toxicity was observed during the 3-wk experiment, and the body weight of the mice showed negligible changes during the treatment period (Fig. 5*E*). Moreover, the blood chemistry test results of mice in the metallacycle treatment group showed no significant variation in liver and kidney functional indices (*SI Appendix*, Fig. S33). Histological examinations of the major organs (heart, liver, spleen, lung, and kidney) showed no obvious abnormalities or lesions after treatment with NPs containing **2** (*SI Appendix*, Fig. S34). These data demonstrate that NPs containing the metallacycle **2** were nontoxic and safe for in vivo applications.

## Conclusions

Two triangular metallacycles (**1** and **2**) were constructed via coordination-driven self-assembly using phenoxy-BODIPY **3** and phenylthio-BODIPY **4** as the building blocks, respectively. The structures of **1** and **2** were confirmed using multinuclear NMR ($^{1}$H and $^{31}$P), ESI-TOF-MS, UV-Vis spectroscopy, and fluorescence spectroscopy. Because of the excellent antitumor ability of the organometallic platinum **5** and the efficient $^{1}O_2$ generation ability of the fluorescent BODIPY **4**, synergistic chemo-photodynamic therapy as well as bioimaging were achieved using **2**. In vitro experiments demonstrated the higher rates of cellular uptake and $^{1}O_2$ generation, and lower $IC_{50}$ value of **2** versus **4**. Furthermore, **2** exerted a stronger antitumor effect in vivo than **4**, indicating that the combination of chemotherapy and PDT results in a synergistic effect. This study provides an alternative strategy for the construction of antitumor drugs with enhanced efficacy through coordination-driven self-assembly.

## Materials and Methods

All reagents and deuterated solvents were commercially available and used as supplied without further purification. Compounds **5** and **6** were synthesized according to the published literature procedures (3, 56). NMR spectra were recorded on a Bruker Advance 500 MHz spectrometer. $^{1}$H and $^{13}$C NMR chemical shifts were reported relative to residual solvent signals, and $^{31}$P{$^{1}$H} NMR chemical shifts were referenced to an external unlocked sample of 85% $H_3PO_4$ ($\delta = 0.0$ ppm). Mass spectra were recorded on Micromass Quattro II triple-quadrupole mass spectrometer and 6530 Q-TOF LC/MS. The melting points were collected on a YRT-3 automatic melting point apparatus. The UV-Vis absorption spectra were measured by a Hitachi U-5300 absorption spectrophotometer. The fluorescent emission spectra were recorded on a Hitachi F-7000 fluorescence spectrophotometer. Transmission electron microscopy (TEM) was performed on a Hitachi F-7700. Dynamic light scattering experiments were performed using a Nano ZS90 instrument with a He-Ne laser (633 nm) and 90° collecting optics. Quantum yields were measured via relative method by using rhodamine B ($\Phi_F = 50\%$ in ethanol, 297 K) as the standard.

The triangular metallacycles (**1** and **2**) were obtained in near quantitative yields (98% for both) by mixing 60° diplatinum(II) acceptor (5) and the corresponding BODIPY ligand (**3** or **4**) in a 1:1 ratio in DMSO and stirring at 50 °C for 12 h.

**Metallacycle 1.** $^{1}$H NMR (500 MHz, DMSO-$d_6$, 297 K): 8.83 (t, 18H), 8.09 (s, 12H), 7.93 (m, 9H), 7.83 (m, 21H), 7.71 (m, 12H), 7.59 (m, 12H), 7.29 (m, 12H), 7.04 (m, 18H), 4.00 (s, 18H), 2.56 (s, 9H), 1.31 (s, 72H), 1.08 (m, 108H). $^{31}$P NMR (202 MHz, DMSO-$d_6$, 297 K): 13.70 ppm (s, $^{195}$Pt satellites, $^{1}J_{Pt\text{-}P} = 2669.4$ Hz). $^{19}$F NMR (471 MHz, DMSO-$d_6$, 297 K): -77.72 (s), -144.43 (m). ESI-TOF-MS: *m/z* 1152.72 [**1** – 5OTf]$^{5+}$, 1478.16 [**1** – 4OTf]$^{4+}$.

**Metallacycle 2.** $^{1}$H NMR (500 MHz, DMSO-$d_6$, 297 K): 8.88–8.81 (m, 18H), 8.10 (s, 12H), 8.89–8.80 (m, 32H), 7.72 (m, 6H), 7.53 (m, 6H), 7.37 (m, 6H), 7.21 (m, 24H), 7.13 (m, 9H), 4.01 (s, 18H), 2.50 (s, 9H), 1.34 (m, 72H), 1.11 (m, 108H). $^{31}$P NMR (202 MHz, DMSO-$d_6$, 297 K): 13.80 ppm (s, $^{195}$Pt satellites, $^{1}J_{Pt\text{-}P} = 2674.9$ Hz). $^{19}$F NMR (471 MHz, DMSO-$d_6$, 297 K): -77.72 (s), -138.28 (m). ESI-TOF-MS: *m/z* 1171.89 [**2** – 5OTf]$^{5+}$, 1502.13 [**2** – 4OTf]$^{4+}$.

**Data Availability.** All study data are included in the article and *SI Appendix*.

**ACKNOWLEDGMENTS.** We are grateful for the financial support from the National Natural Science Foundation of China (grant numbers 21971049 and 51903070) and "Ten-thousand Talents Plan" of Zhejiang Province (grant number 2019R52040).

1. F. Bray *et al.*, Global cancer statistics 2018: GLOBOCAN estimates of incidence and mortality worldwide for 36 cancers in 185 countries. *CA Cancer J. Clin.* **68**, 394–424 (2018).
2. D. Chen *et al.*, pH-responsive PEG-doxorubicin-encapsulated Aza-BODIPY nanotheranostic agent for imaging-guided synergistic cancer therapy. *Adv. Healthc. Mater.* **7**, e1701272 (2018).
3. Y. Li *et al.*, Amphiphilic rhomboidal organoplatinum(II) metallacycles with encapsulated doxorubicin for synergistic cancer therapy. *ACS Appl. Bio Mater.* **3**, 8061–8068 (2020).
4. Y. Fan *et al.*, Amphiphilic rhomboidal metallacycles with aggregation-induced emission and aggregation-caused quenching luminogens for white-light emission and bioimaging. *Mater. Chem. Front.* **6**, 633–643 (2022).
5. C. He, D. Liu, W. Lin, Self-assembled core-shell nanoparticles for combined chemotherapy and photodynamic therapy of resistant head and neck cancers. *ACS Nano* **9**, 991–1003 (2015).
6. W. Hu *et al.*, Engineering lysosome-targeting BODIPY nanoparticles for photoacoustic imaging and photodynamic therapy under near-infrared light. *ACS Appl. Mater. Interfaces* **8**, 12039–12047 (2016).
7. W. Wu *et al.*, Enhancing selective photooxidation through Co–Nx-doped carbon materials as singlet oxygen photosensitizers. *ACS Catal.* **7**, 7267–7273 (2017).
8. V. Ramu, S. Gautam, A. Garai, P. Kondaiah, A. R. Chakravarty, Glucose-appended platinum(ii)-BODIPY conjugates for targeted photodynamic therapy in red light. *Inorg. Chem.* **57**, 1717–1726 (2018).
9. L. Sansalone *et al.*, A photoactivatable far-red/near-infrared BODIPY to monitor cellular dynamics in vivo. *ACS Sens.* **3**, 1347–1353 (2018).
10. X. Zhang *et al.*, Light-enhanced hypoxia-response of conjugated polymer nanocarrier for successive synergistic photodynamic and chemo-therapy. *ACS Appl. Mater. Interfaces* **10**, 21909–21919 (2018).
11. S.-Z. Ren *et al.*, Oxygen self-sufficient core-shell metal-organic framework-based smart nanoplatform for enhanced synergistic chemotherapy and photodynamic therapy. *ACS Appl. Mater. Interfaces* **12**, 24662–24674 (2020).
12. M. Lan *et al.*, Photosensitizers for photodynamic therapy. *Adv. Healthc. Mater.* **8**, e1900132 (2019).
13. J. Zou *et al.*, BODIPY derivatives for photodynamic therapy: Influence of configuration versus heavy atom effect. *ACS Appl. Mater. Interfaces* **9**, 32475–32481 (2017).
14. A. Kamkaew *et al.*, BODIPY dyes in photodynamic therapy. *Chem. Soc. Rev.* **42**, 77–88 (2013).
15. S. Ye *et al.*, Rational design of conjugated photosensitizers with controllable photoconversion for dually cooperative phototherapy. *Adv. Mater.* **30**, e1801216 (2018).
16. M. Zhao *et al.*, Halogenated Aza-BODIPY for imaging-guided synergistic photodynamic and photothermal tumor therapy. *Adv. Healthc. Mater.* **7**, e1800606 (2018).
17. T. Zhang, C. Ma, T. Sun, Z. Xie, Unadulterated BODIPY nanoparticles for biomedical applications. *Coord. Chem. Rev.* **390**, 76–85 (2019).
18. J. Zou *et al.*, Penetration depth tunable BODIPY derivatives for pH triggered enhanced photothermal/photodynamic synergistic therapy. *Chem. Sci. (Camb.)* **10**, 268–276 (2018).
19. D. Chen *et al.*, Boosting O2●− Photogeneration via promoting intersystem-crossing and electron-donating efficiency of Aza-BODIPY-based nanoplatforms for hypoxic-tumor photodynamic therapy. *Small Methods* **4**, 2000013 (2020).
20. M. Yoshizawa, J. K. Klosterman, M. Fujita, Functional molecular flasks: New properties and reactions within discrete, self-assembled hosts. *Angew. Chem. Int. Ed. Engl.* **48**, 3418–3438 (2009).
21. R. Chakrabarty, P. S. Mukherjee, P. J. Stang, Supramolecular coordination: Self-assembly of finite two- and three-dimensional ensembles. *Chem. Rev.* **111**, 6810–6918 (2011).
22. T. R. Cook, Y.-R. Zheng, P. J. Stang, Metal-organic frameworks and self-assembled supramolecular coordination complexes: Comparing and contrasting the design, synthesis, and functionality of metal-organic materials. *Chem. Rev.* **113**, 734–777 (2013).
23. Y.-Y. Zhang *et al.*, Supramolecular polymer networks with enhanced mechanical properties: The marriage of covalent polymer and metallacycle. *Chin. J. Chem.* **39**, 2731–2737 (2021).
24. F. Chen *et al.*, Metallacycle-crosslinked supramolecular polymers constructed by amino-YNE click reaction with enhanced mechanical properties. *Supramol. Mater.* **1**, 100003 (2022).
25. H. Zhu *et al.*, Dual-emissive platinum(II) metallacage with a sensitive oxygen response for imaging of hypoxia and imaging-guided chemotherapy. *Angew. Chem. Int. Ed. Engl.* **59**, 20208–20214 (2020).
26. S. Li *et al.*, Self-assembly of triangular and hexagonal molecular necklaces. *J. Am. Chem. Soc.* **136**, 5908–5911 (2014).
27. Z. Zhou *et al.*, Immobilizing tetraphenylethylene into fused metallacycles: Shape effects on fluorescence emission. *J. Am. Chem. Soc.* **138**, 13131–13134 (2016).
28. C. M. Hong, D. M. Kaphan, R. G. Bergman, K. N. Raymond, F. D. Toste, Conformational selection as the mechanism of guest binding in a flexible supramolecular host. *J. Am. Chem. Soc.* **139**, 8013–8021 (2017).
29. H. Sepehrpour, M. L. Saha, P. J. Stang, Fe-Pt twisted heterometallic bicyclic supramolecules via multicomponent self-assembly. *J. Am. Chem. Soc.* **139**, 2553–2556 (2017).
30. M. Zhang *et al.*, Metallacycle-cored supramolecular assemblies with tunable fluorescence including white-light emission. *Proc. Natl. Acad. Sci. U.S.A.* **114**, 3044–3049 (2017).
31. S. Datta, M. L. Saha, P. J. Stang, Hierarchical assemblies of supramolecular coordination complexes. *Acc. Chem. Res.* **51**, 2047–2063 (2018).
32. Y. Fang *et al.*, Ultra-small face-centered-cubic Ru nanoparticles confined within a porous coordination cage for dehydrogenation. *Chem* **4**, 555–563 (2018).
33. S. Komine, S. Takahashi, T. Kojima, H. Sato, S. Hiraoka, Self-assembly processes of octahedron-shaped $Pd_6L_4$ cages. *J. Am. Chem. Soc.* **141**, 3178–3186 (2019).
34. H. Takezawa, R. Tabuchi, H. Sunohara, M. Fujita, Confinement of water-soluble cationic substrates in a cationic molecular cage by capping the portals with tripodal anions. *J. Am. Chem. Soc.* **142**, 17919–17922 (2020).
35. X. Wang *et al.*, Biotinylated platinum(ii) metallacage towards targeted cancer theranostics. *Chem. Commun. (Camb.)* **56**, 8460–8463 (2020).
36. C. J. Hastings, M. D. Pluth, R. G. Bergman, K. N. Raymond, Enzymelike catalysis of the Nazarov cyclization by supramolecular encapsulation. *J. Am. Chem. Soc.* **132**, 6938–6940 (2010).
37. C. Lu *et al.*, Fluorescent metallacage-core supramolecular polymer gel formed by orthogonal metal coordination and host-guest interactions. *J. Am. Chem. Soc.* **140**, 7674–7680 (2018).
38. K. Acharyya *et al.*, Self-assembled fluorescent Pt(II) metallacycles as artificial light-harvesting systems. *J. Am. Chem. Soc.* **141**, 14565–14569 (2019).
39. X. Chang *et al.*, Coordination-driven self-assembled metallacycles incorporating pyrene: Fluorescence mutability, tunability, and aromatic amine sensing. *J. Am. Chem. Soc.* **141**, 1757–1765 (2019).
40. B. Shi *et al.*, Spontaneous formation of a cross-linked supramolecular polymer both in the solid state and in solution, driven by platinum(II) metallacycle-based host-guest interactions. *J. Am. Chem. Soc.* **141**, 6494–6498 (2019).
41. B. Shi *et al.*, Spontaneous supramolecular polymerization driven by discrete platinum metallacycle-based host-guest complexation. *J. Am. Chem. Soc.* **141**, 11837–11841 (2019).
42. Q. Zhang *et al.*, Self-healing heterometallic supramolecular polymers constructed by hierarchical assembly of triply orthogonal interactions with tunable photophysical properties. *J. Am. Chem. Soc.* **141**, 17909–17917 (2019).
43. Z. Zhou *et al.*, Designed conformation and fluorescence properties of self-assembled phenazine-cored platinum(II) metallacycles. *J. Am. Chem. Soc.* **141**, 5535–5543 (2019).
44. S. Bhattacharyya *et al.*, Self-assembled $Pd_{12}$ coordination cage as photoregulated oxidase-like nanozyme. *J. Am. Chem. Soc.* **142**, 18981–18989 (2020).
45. T. Hong *et al.*, Chiral metallacycles as catalysts for asymmetric conjugate addition of styrylboronic acids to α,β-enones. *J. Am. Chem. Soc.* **142**, 10244–10249 (2020).
46. Y.-X. Hu *et al.*, Construction of supramolecular liquid-crystalline metallacycles for holographic storage of colored images. *J. Am. Chem. Soc.* **142**, 6285–6294 (2020).
47. M. Zhang *et al.*, Fluorescent metallacycle-cored polymers via covalent linkage and their use as contrast agents for cell imaging. *Proc. Natl. Acad. Sci. U.S.A.* **113**, 11100–11105 (2016).
48. G. Yu *et al.*, A discrete organoplatinum(II) metallacage as a multimodality theranostic platform for cancer photochemotherapy. *Nat. Commun.* **9**, 4335 (2018).
49. Y. Sun *et al.*, Melanin-dot-mediated delivery of metallacycle for NIR-II/photoacoustic dual-modal imaging-guided chemo-photothermal synergistic therapy. *Proc. Natl. Acad. Sci. U.S.A.* **116**, 16729–16735 (2019).
50. G. Yu *et al.*, Tetraphenylethene-based highly emissive metallacage as a component of theranostic supramolecular nanoparticles. *Proc. Natl. Acad. Sci. U.S.A.* **113**, 13720–13725 (2016).
51. G. Yu *et al.*, Antitumor activity of a unique polymer that incorporates a fluorescent self-assembled metallacycle. *J. Am. Chem. Soc.* **139**, 15940–15949 (2017).
52. J. Zhou *et al.*, Highly emissive self-assembled BODIPY-platinum supramolecular triangles. *J. Am. Chem. Soc.* **140**, 7730–7736 (2018).
53. W. Heng, C. Guo, X. Li, Multidimensional mass spectrometry assisted metallo-supramolecular chemistry. *CCS Chemistry* **3**, 3161–3184 (2021).
54. R. W. Redmond, J. N. Gamlin, A compilation of singlet oxygen yields from biologically relevant molecules. *Photochem. Photobiol.* **70**, 391–475 (1999).
55. J. Zou *et al.*, Singlet oxygen "afterglow" therapy with NIR-II fluorescent molecules. *Adv. Mater.* **33**, e2103627 (2021).
56. M. J. Ortiz *et al.*, Synthesis and functionalization of new polyhalogenated BODIPY dyes. Study of their photophysical properties and singlet oxygen generation. *Tetrahedron* **68**, 1153–1162 (2012).